ORIGINAL RESEARCH ARTICLE

The Impact Abrasive Wear Resistance and Mechanical Properties of In Situ NbC-Reinforced H13 Steel Composites

Zhou Liu, Mojin Zhou, Yehua Jiang, and Zhijie Wang

H13 steel is a common material for the cutter ring of tunnel boring machines, and it can affect the engineering cycle due to its high wear loss during work. In order to improve the wear resistance of the H13 steel, NbC-reinforced H13 matrix composites were prepared through in-situ casting method. The results showed that the NbC phase had a reticular structure when the content of NbC was 1 vol.%. It gradually changed from such structure to rod-like and granular as the content was increased to 3 and 5 vol.%, respectively. The hardness and elastic modulus of NbC reached the maximum of 8.1 ± 0.9 and 246.8 ± 6.7 GPa, respectively. As its content grew higher, it reduced the mechanical properties of the composites, whose yield strength and elongation were 266.7 MPa and 2.6%, respectively. The high-stress impact abrasive wear tests showed that the wear resistance of the composites was at least 1.12 times higher than that of the NbC-free H13 composite. The wear mechanisms of the composites were micro-cutting and fracture spalling of NbC.

1. Introduction

A tunnel boring machine (TBM) is a machine used to excavate hard rock tunnels for large-scale construction, such as water tunnels, subway tunnels, and highway tunnels(Ref 1-3). During tunnel excavation, the cutter ring is a key component for TBM to break rock (Ref 4). The cutter ring is subject to impact abrasive wear in work (Ref 5, 6). According to statistics, the cost caused by cutter ring wear accounts for one-third of the total construction cost (Ref 7, 8). The wear resistance of materials depends not only on the strength and hardness, but also on their microstructural characteristics, which play a dominant role in resisting abrasive wear (Ref 9, 10). With good designability, high hardness, high modulus, and high wear resistance, steel matrix composites modified with ceramic particles have been used in some key components that require high wear resistance. The composites have replaced traditional wear-resistant steel composites (Ref 11-14). Generally, WC,

Al$_2$O$_3$, SiC, ZTA, and TiC ceramic particles are used to reinforce composites (Ref 15). WC ceramic particles have good wettability with molten iron and can produce high interfacial bond strength. The coefficient of linear thermal expansion (CTE) of WC and that of the steel matrix is so different that they can hardly match in physical properties (Ref 16). Al$_2$O$_3$ particles are widely used for industrial production because of their low price, high hardness, and good wear resistance. But they have poor wettability with Fe, thus bringing weak interfacial bond strength (Ref 17). SiC ceramic particles have good thermal conductivity, and their CTE is close to that of the steel matrix. However, show that they can react with molten iron violently, which leads to brittle ferrosilicon compounds and flake graphite structures on the surface and damage it (Ref 18). ZTA ceramic particles have high hardness and their CTE is close to Fe, which is an ideal ceramic-reinforcing choice. But they also have some disadvantages, such as poor wettability with Fe, poor interfacial bond strength with the matrix and prone to surface cracks and debonded interfaces (Ref 19). TiC particles have a low density and their inclusions reduce the overall density of composites. The density difference may cause these particles to float and distribute unevenly during casting and solidification (Ref 20, 21).

Niobium carbide (NbC) has excellent properties such as high hardness, high melting point (3610 °C), high elastic modulus, as well as good wear resistance and chemical stability. With good wettability, its density is similar to molten iron and steel (Ref 22, 23). Thus it distributes in steel or iron matrix uniformly and brings good interfaces, which solves the problems above (Ref 24, 25). Composites can be prepared by using the external addition method and the in-situ casting method. Compared with common externally reinforced particles, the particles produced by in-situ reactions have obvious advantages. The interface between ceramic particles and the matrix, for instance, is clean, pollution-free, and moist. It has

Zhou Liu, Faculty of Mechanical and Electrical Engineering, Kunming University of Science and Technology, Kunming 650000, People's Republic of China; **Mojin Zhou** and **Zhijie Wang**, School of Materials Science and Engineering, Kunming University of Science and Technology, Kunming 650000, People's Republic of China; and **Yehua Jiang**, National and Local Joint Engineering Laboratory of Advanced Metal Solidification Forming and Equipment Technology, Kunming University of Science and Technology, Kunming 650000, People's Republic of China. Contact e-mail: zhoumojin@kmust.edu.cn.

good wettability, high interfacial bond strength, a relatively simple preparation process, and low cost, and it only requires a small amount to reinforce composites (Ref 26, 27). Studies show that iron matrix composites reinforced with NbC particles can be prepared in situ by using the infiltration casting and heat treatment method. The addition of in-situ NbC particles greatly improves the micro-hardness of gray casting iron (Ref 28). The AISI 440B martensitic stainless steel modified with 15 vol.% NbC particles was cast by researchers in a vacuum induction furnace, and it was found that NbC particles improve the sliding wear resistance and corrosion resistance of the composites (Ref 29). A new type of Nb-reinforced low-alloy steel with wear resistance has been developed by predecessors. Compared with the alloy steel without Nb, the one containing 0.05 wt.% Nb has higher strength properties and better impact wear properties (Ref 30). Chao et al. (Ref 31) synthesised TaC particle-reinforced Ni-based composite coatings in situ on mild steel by laser melting, which significantly improve the micro-hardness and wear resistance of the composites. Inspired by this, Wang et al.(Ref 32) prepared Ti-based composite coatings modified by NbC particles generated in situ by laser melting, and the result showed that NbC particles greatly improved the wear resistance of the coatings.

However, the CTE difference between coatings and the matrix makes coatings susceptible to cracking and peeling, which in turn reduces the service life of the composites. In this paper, therefore, NbC/H13 steel composites were prepared through in-situ gravity casting, which is a good solution to the problem of poor bond strength between ceramic particles and the matrix. The effects on microstructure, mechanical properties, and impact abrasive wear properties of NbC/H13 steel composites with different NbC volume fractions were studied.

2. Experimental Methods

2.1 Composites Preparation

H13 steel composites reinforced with in-situ NbC particles were prepared through casting. A 150 kg medium-frequency induction furnace was used for melting. The matrix was melted with oxide-free # 45 steel, high-carbon ferro-chrome (57 wt.% Cr), low-carbon ferro-chrome (60 wt.% Cr), ferro-molybdenum (58 wt.% Mo), ferro-vanadium (50 wt.% V), ferro-manganese (65 wt.% Mn), ferro-silicon (73 wt.% Si), and scrap (98 wt.% Fe). The composites were made by adding ferro-niobium (65 wt%Nb) to molten steel to replace Nb particles. The molten steel was slagge before being removed from the furnace at 1600 ± 15 °C, deoxidized with Al wire, and poured into a sand cavity. The specimen moulds have standard Keelblock sizes, and their locations are shown in Fig. 1.

The approximate mass fraction of Nb in the bulk can be worked out based on the following formula (Ref 25):

Approximate mass fraction of NbC vol.% = 1.13 Nb wt.%
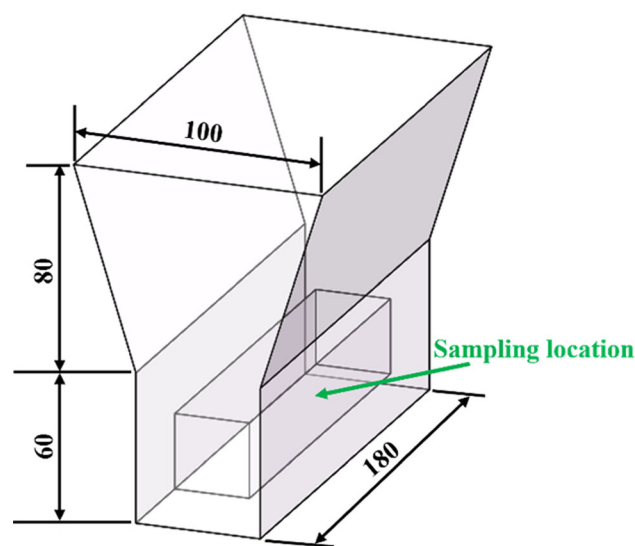
$$\text{(Eq 1)}$$

Fig. 1 Keelblock sizes and location of the moulds

The coefficient 1.13 in Eq 1 is the ratio of the atomic weights of NbC and Nb. The chemical composition of composites containing different NbC was determined by a direct-reading spectrum analyzer (ARL4460), as shown in Table 1.

According to the phase diagram of the Fe-C and Nb-C alloys, the following three chemical reactions may occur during the in-situ generation of NbC.

$$[\text{Nb}] + [\text{C}] = \text{NbC(s)} \tag{Eq 2}$$

$$2[\text{Nb}] + [\text{C}] = \text{Nb}_2\text{C(s)} \tag{Eq 3}$$

$$3[\text{Fe}] + [\text{C}] = \text{Fe}_3\text{C(s)} \tag{Eq 4}$$

The Gibbs free enthalpy worked out by Wang et al. (Ref 33) shows that ΔG_{NbC} is negative only at 1600 ± 15 °C, indicating that the reaction can proceed spontaneously at this temperature. In the Fe-Nb-C stell, the Nb atom has a stronger binding ability with the C atom than the Fe atom under the same conditions, leading to the preferential formation of NbC. Even if a small amount of Fe_3C is produced, it gradually decomposes into Fe and C during the cooling process, so no harmful Fe_3C phase appears in the preparation of the NbC/H13 steel composites.

2.2 Microstructural Characterization

The microstructure and wear morphology of the composites were observed by a scanning electron microscope (SEM, ZEISS-EVO18). The sample surfaces were polished and then etched with 4 vol.% nitric acid alcohol solution for 5-10 s for microstructure observation. The phase composition of the samples was determined by an x-ray diffractometer (XRD, D/max-2500). The sizes of micron-scale phases were measured by a high-resolution transmission electron microscope (HR-

Table 1 Chemical composition of steel with different Nb (wt.%)

Specimen	Element, wt.%									
	Nb	C	Si	Mn	Mo	Cr	V	Fe	P	S
NbC-free	…	0.37	1.03	0.26	1.23	5.06	1.11	Bal.	≤ 0.03	≤ 0.03
1 vol.% NbC	0.96	0.39	1.12	0.25	1.28	5.12	1.07	Bal.	≤ 0.03	≤ 0.03
3 vol.% NbC	2.75	0.40	1.17	0.27	1.24	4.94	1.03	Bal.	≤ 0.03	≤ 0.03
5 vol.% NbC	4.65	0.44	1.08	0.34	1.31	5.22	1.15	Bal.	≤ 0.03	≤ 0.03
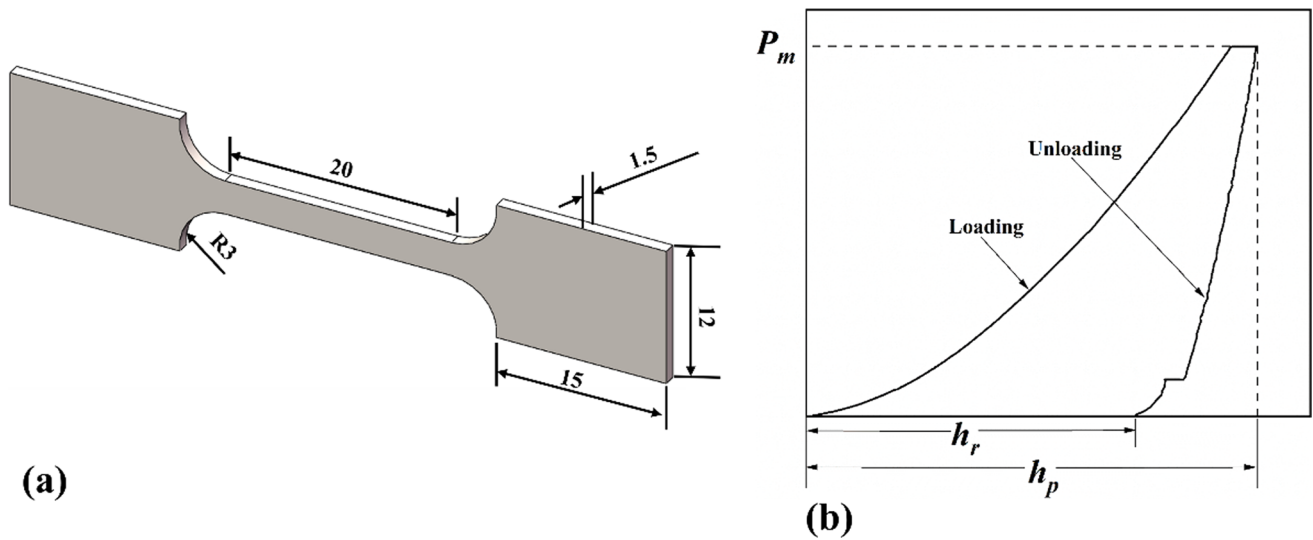
Fig. 2 (a) Shape and size of the tensile specimen and (b) load-depth curve of nanoindentation

TEM, FEI Tecnai G2 TF30). The films used for HR-TEM testing were mechanically thinned to 0.08 mm and then perforated in an electrolytic double injection solution with 6 vol.% perchloric acid in ethanol at − 25 °C. Electron probe microanalysis (EPMA, SHIMADZU EPMA-1720) was used to analyze the chemical composition of carbides formed in the composites.

2.3 Mechanical Property Testing

The tensile properties of the composites were tested in a WH-5000 universal testing machine based on the GBT228.1-2010 standard. The tensile rate was 1 mm/min and the size of the samples was shown in Fig. 2(a). To ensure the accuracy of the ultimate tensile strength (UTS), yield strength (YS), and elongation results during the research, there were three parallel samples in each experiment, and the results were the average of three values. A Hysitron Ti950 Triboindenter nanoindenter was used to characterize the mechanical properties of the NbC-free composite and the NbC phase. The load depth curve is shown in Fig. 2(b). P_m represents the maximum load during the indentation process, h_p the indentation depth under the maximum load, h_r the indentation depth after unloading, h_p-h_r the recovery depth, and ε_r the relative elastic recovery rate. The calculation formula is as follows (Ref 34):

$$\varepsilon_r = \frac{h_p - h_r}{h_p} \tag{Eq 5}$$

All indentation experiments were carried out under a test force of 50 mN and a dwell time of 10 s.

2.4 Characterization of Hardness and Wear Properties

The samples received impact abrasive wear tests on an MLD-10 impact wear machine, as shown in Fig. 3(a). Then the sample in the upper part was cut into 10 mm × 10 mm × 30 mm cuboids. The weight of the hammer was 10 kg, and the impact energy could be adjusted by changing the drop height of the hammer. The abrasive shown in Fig. 3(b) was quartz sand with a size of 40 -70 mesh. The flow rate of the abrasives was 30 kg/h, and the sample in the upper part was impacted at 60 times/min, while that at the lower part was rotated at 200 rpm. In the impact abrasive wear tests, the impact energy
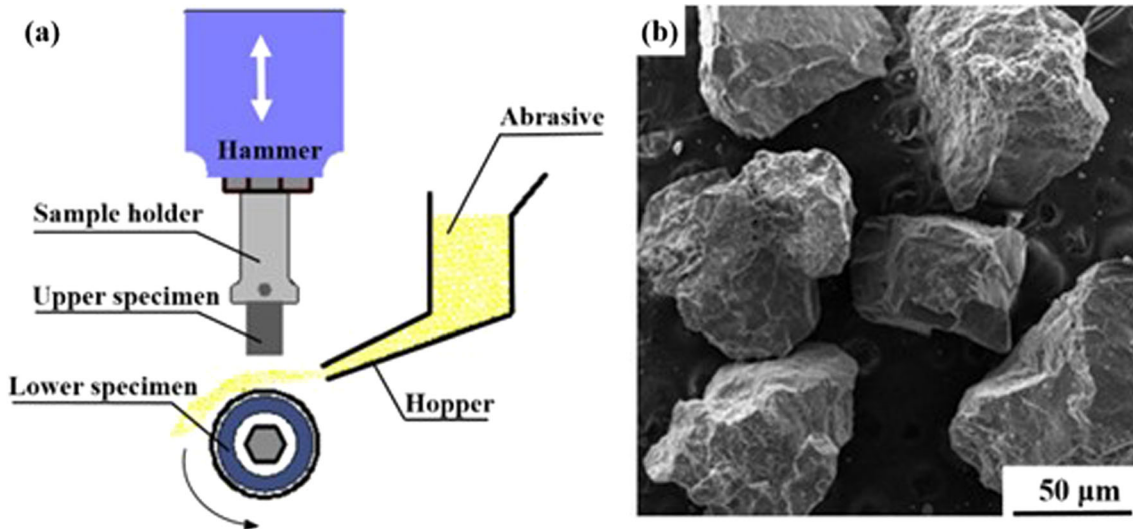
Fig. 3 (a) Schematic illustration of the three-body abrasive wear test and (b) SEM morphology of the abrasive
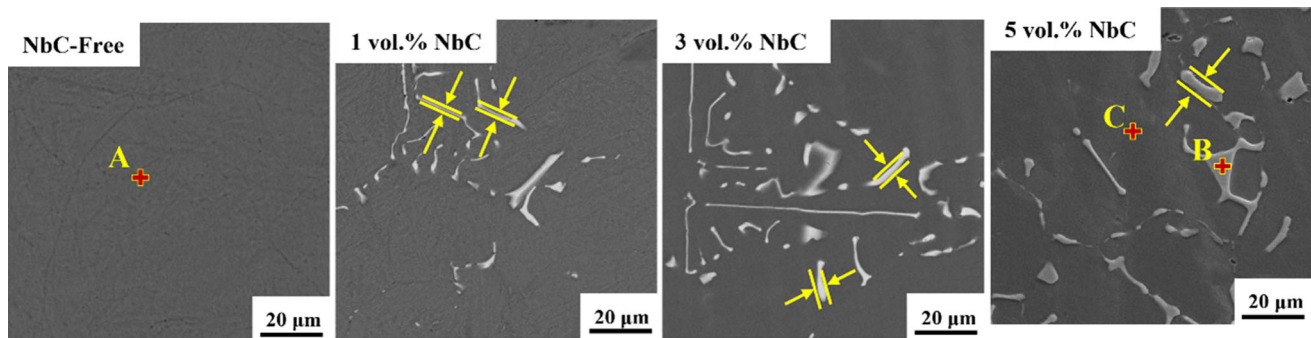

Fig. 4 SEM images and elemental distribution of NbC/H13 steel composites with different volume fractions

Table 2 EDS analysis results for the points in Fig. 4 (at.%)

Point	Cr	Fe	Si	V	Mn	Mo	Nb
A	4.7	91.9	0.9	0.9	0.3	1.1	0
B	0	2.4	0	1.3	0	0	96.3
C	5.0	91.2	1.2	1.0	0.5	1.1	0

was set at 5 J to simulate the impact abrasive wear under high-stress loading. To ensure repeatability, the samples were tested three times. Before the start of the tests, the pre-wear was performed for 10 min to ensure that the specimen in the upper part had a stable wear contact surface. The samples were taken out every 10 min and placed in an ultrasonic cleaner for cleaning. Then, they were weighed by a precision electronic balance (with an accuracy of 0.01 mg) to figure out the weight loss caused by 10 min grinding and convert it to volume loss.

3. Results and Discussion

3.1 Microstructure

Figure 4 shows the SEM images of NbC/H13 steel composites with different volume fractions. As can be seen from the figure, some white phases exist in the gray matrix in the shapes of particles, small rods, and reticular structures. Table 2 shows the composition of points A, B, and C in Fig. 4. The mapping results show that Nb was mainly located in the white phases.

In the 1 vol.% NbC/H13 steel composite, a white phase can be observed with a reticular structure morphology along the dendrite arms. But in the 3 and 5 vol.% NbC/H13 steel composites, they are rodlike and granular. As the content of Nb grows higher, the size and number of small rods gradually increase and small rods gradually change to granular. The 3 vol.% NbC/H13 steel composite has fewer coarse white phases, which were attributed to Ostwald ripening, than the 5 vol.% one (Ref 35).
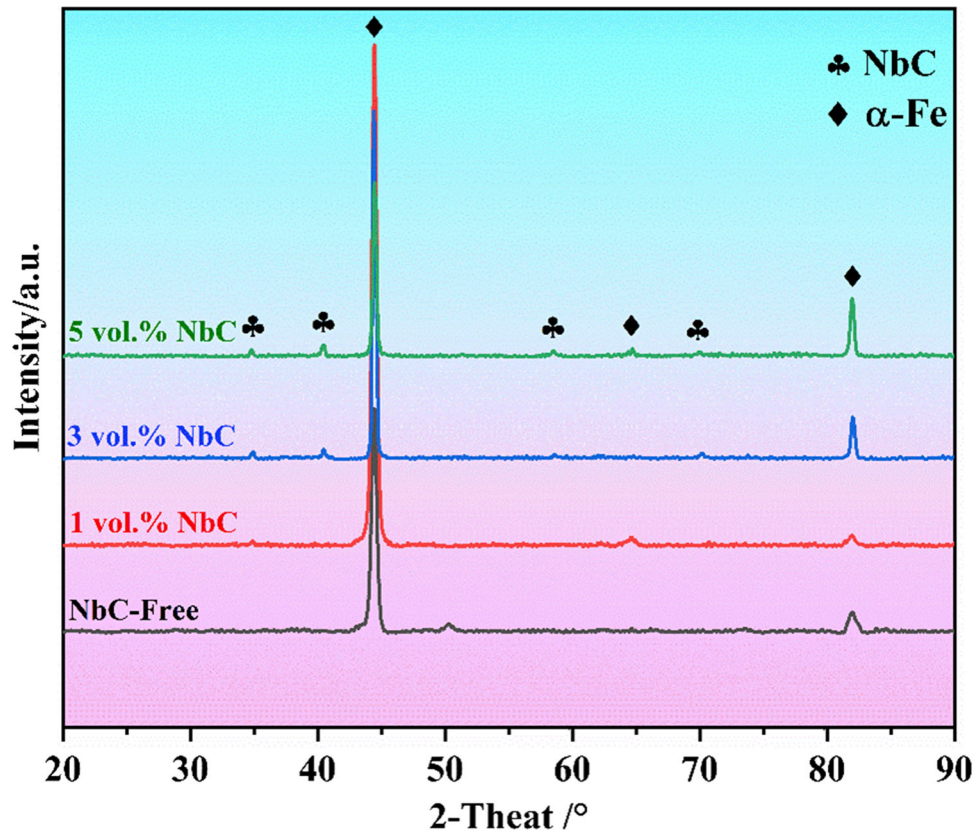
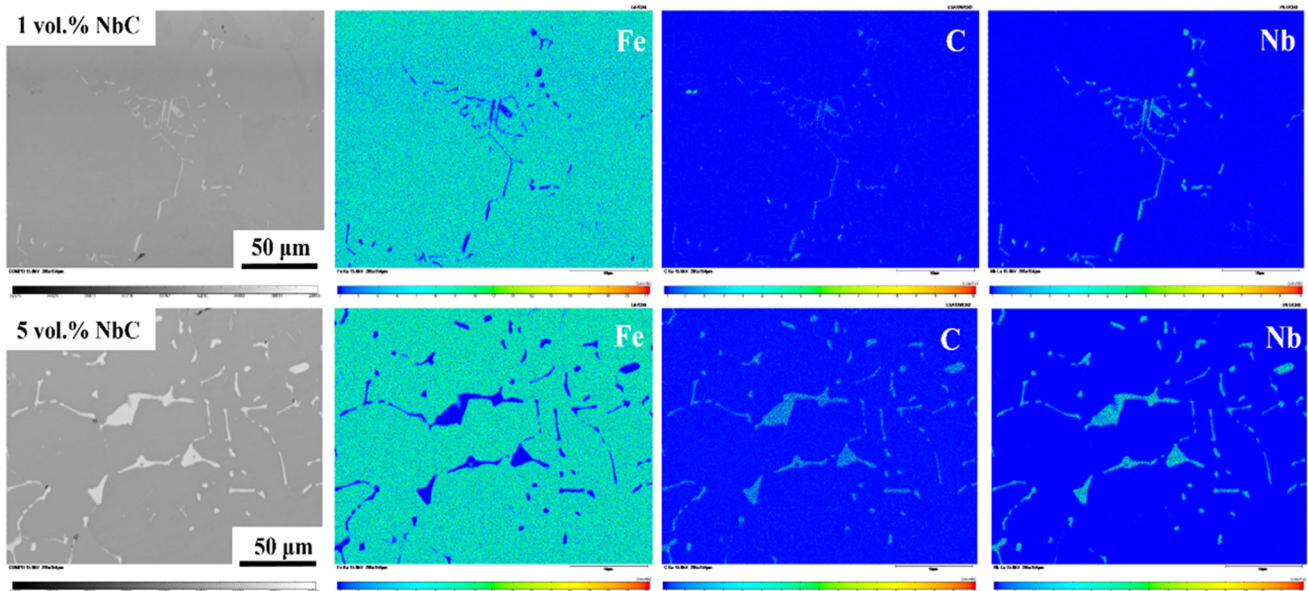**Fig. 5** XRD of H13 steel and NbC/H13 steel composites

Fig. 6 EPMA images of 1 vol.% NbC/H13 steel composites and 5 vol.% NbC/H13 steel composites

Figure 5 shows the XRD analysis results of the composites. It can be seen that the main phase in H13 steel was α-Fe. NbC was formed in the composites by an in-situ reaction. As the volume fraction of NbC increased, the peaks of NbC became higher. Trace phases of alloyed carbides in the matrix are not shown in the XRD results because these alloying and non-alloying elements exist in the α-Fe in the form of solid solutions, not compounds or something else.

Figure 6 shows the EPMA diagrams of Fe, C, and Nb distribution in 1 vol.% NbC and 5 vol.% NbC composites, respectively. C and Nb distribute in the same area. The white area was proved to contain NbC after an XRD analysis. After a
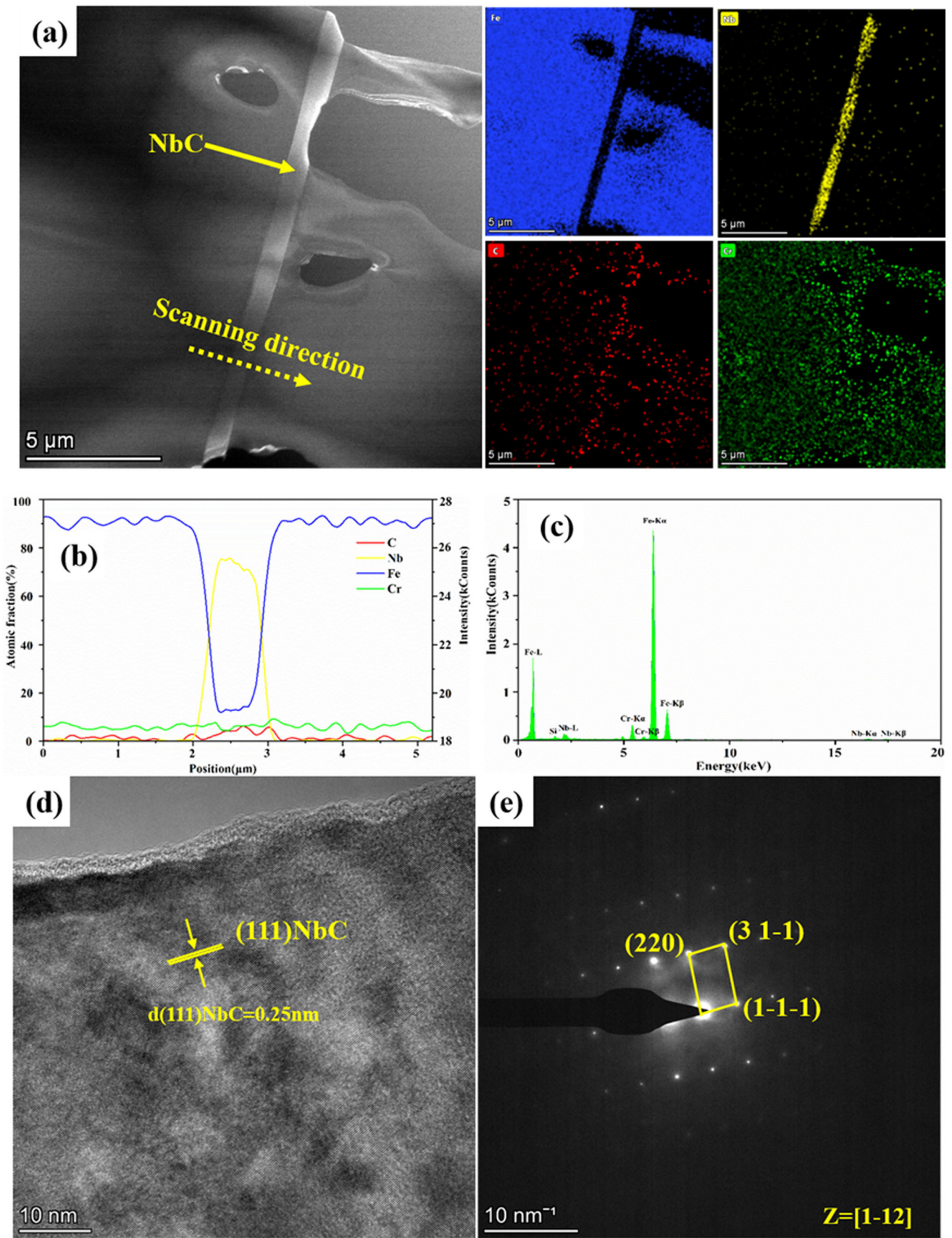
Fig. 7 (a) TEM image of the 3 vol.% NbC composite; (b) its line scanning image; (c) its energy total spectrum image; (d) its HR-TEM image; (e) its SADP pattern
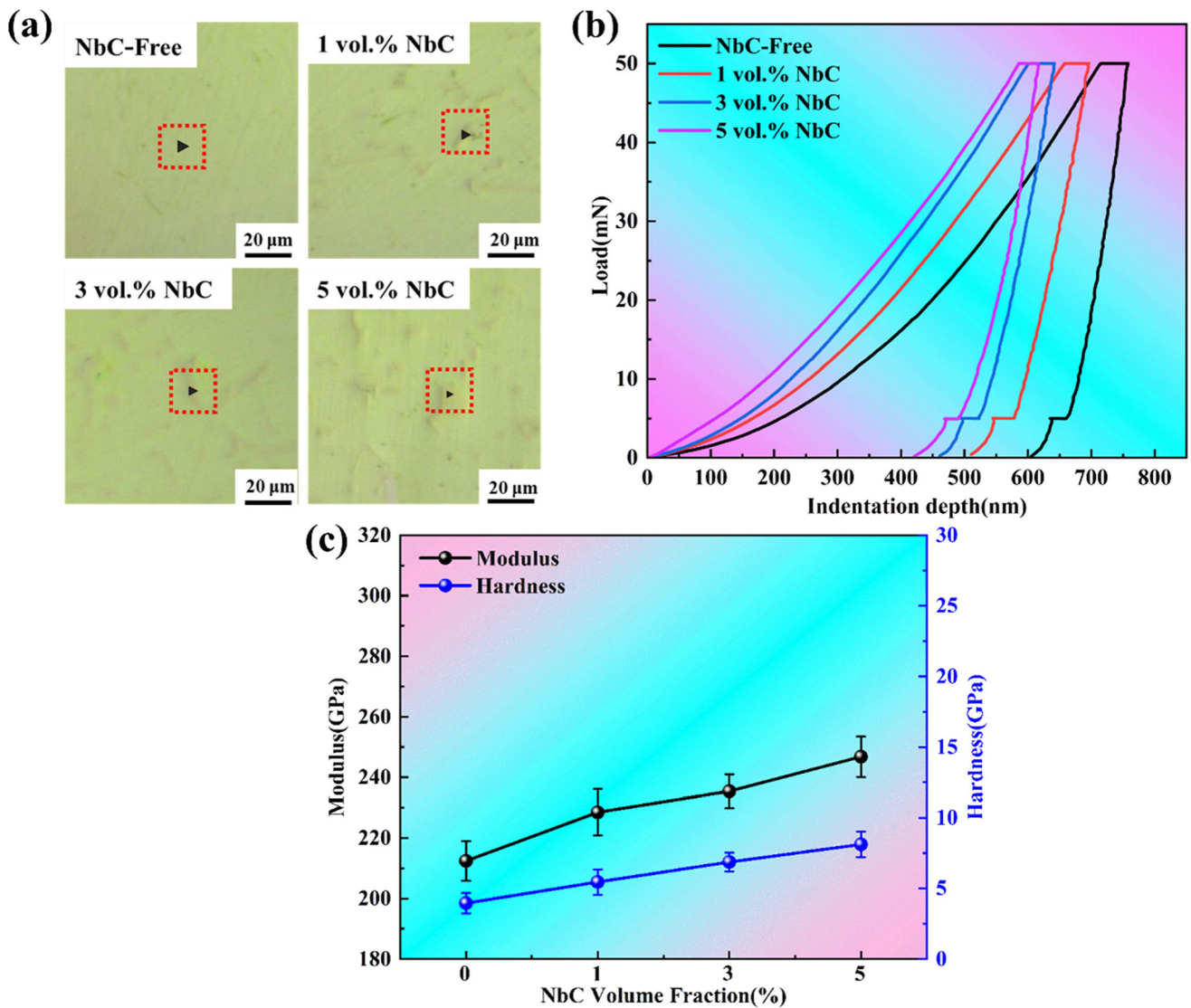
Fig. 8 Indentation results of NbC/H13 steel composites with different volume fractions: (a) test position diagram of indentation; (b) load-depth curve; (c) hardness and elastic modulus of each specimen point

Table 3 h_p, h_r, ε_r, hardness, modulus in different test points

Sample	h_p, nm	h_r, nm	ε_r, %	Hardness, GPa	Modulus, GPa
NbC-Free	757	502.3	33.7	3.9 ± 0.7	212.4 ± 6.5
1 vol.% NbC	696	436.6	37.3	5.5 ± 0.8	228.5 ± 7.7
3 vol.% NbC	639	391.3	38.8	6.9 ± 0.7	235.4 ± 5.6
5 vol.% NbC	617	362.5	41.3	8.1 ± 0.9	246.8 ± 6.7

comparison of the distribution of Fe and C, the matrix area was found to contain much Fe, which was consistent with the XRD results.

In order to further analyze the structure and interface of NbC/H13 steel composites, TEM tests were carried out on the 3 vol.% NbC composite, and the results are shown in Fig. 7. Obviously, NbC particles distribute in the Fe matrix in the

shape of rods. Linear scanning was carried out from NbC particles to the matrix (Fig. 7b), and it suggested that the transition between Fe and Nb was good. Figure 7(d) and (e) shows the HR-TEM images of the micron NbC particles and their selected area electron diffraction (SAED). The phase with the function of modification is determined to be NbC based on the fast Fourier transform (FFT) diffraction pattern and the
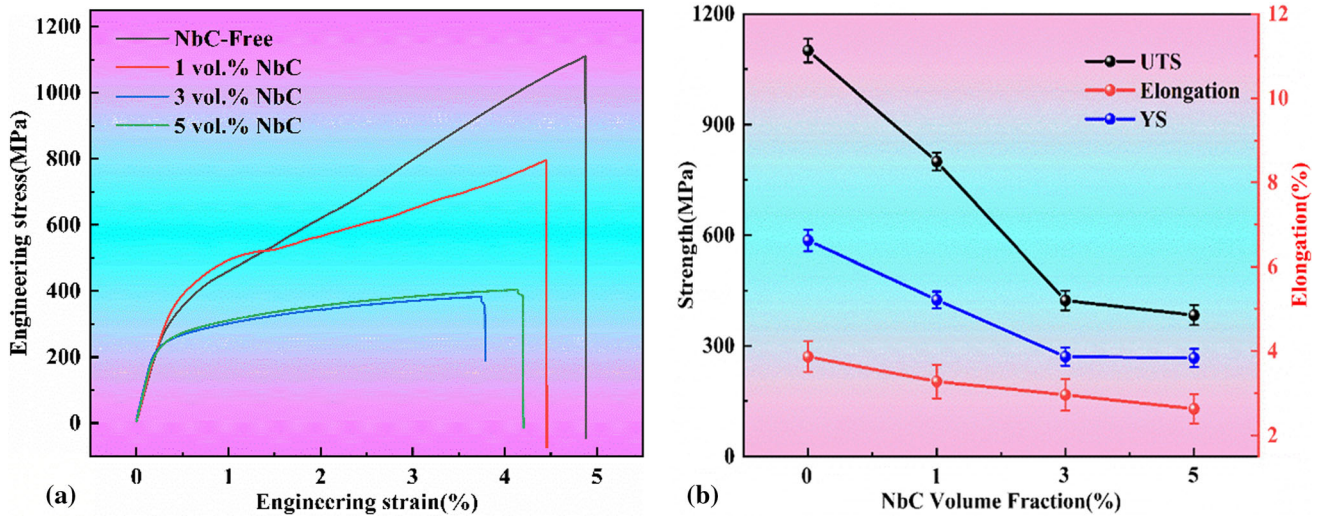
Fig. 9 Mechanical properties of NbC/H13 steel composites with different volume fractions

SAED results. The atomic space of NbC is 0.25 nm, as shown in Fig. 7(d).

3.2 Nanoindentation Results

The nanoindentation results of NbC/H13 composites with different NbC volume fractions are shown in Fig. 8. The h_p, h_r, ε_r, hardness and elastic modulus are shown in Table 3. Figure 8(a) and (b) shows the indentation location and load depth curves. The indentation size of the NbC phase is found smaller, and its maximum penetration depth (hp) and the remaining indentation depth (hr) are significantly shallower than that of the matrix. Under the same load, the matrix undergoes greater plastic deformation than the NbC phase. This means the NbC phase made the composite more resistant to plastic deformation. The hardness and elastic modulus in Fig. 8(c) gradually increase with the volume fraction of NbC. Compared to the NbC-free H13 steel, the 5 vol.% NbC one has seen its hardness increase by 51.4% and modulus by 13.9%. Based on Eq 5, the relative elastic recovery rates ε_r of the matrix and the NbC phase after unloading were calculated. The relative elastic recovery rate of the matrix is lower than the NbC phase. The relative elastic recovery rate gradually increases with the volume fraction of NbC, which has good elastic-plastic properties (Ref 36).

3.3 Mechanical Properties and Fracture Analysis

As with most metal matrix composites, the addition of ceramic particles to the steel matrix typically results in reduced ductility and toughness in exchange for higher hardness and wear resistance (Ref 37). Tensile tests were performed on the composites to verify the combined mechanical properties of each composite. Figure 9 shows the change in tensile properties of different composites. The shape of NbC is non-regular when subjected to external forces. Cracks are easy to appear and expand when the NbC stress is concentrated. The NbC phase destroys the continuity of the matrix, resulting in a decrease in the strength of the composites. As the NbC phase grows larger, it is more likely to have stress concentrations and the strength is reduced faster. The experimental results show that ceramic-particle composites with high tensile strength and metal matrix experienced worse deformation during the tensile process. Compared with the pure matrix, the composites have a lower shape variable. The deformation of the pure matrix is 4.9%, while the tensile deformation of the composites with ceramic particles is 3.8%. In addition, the UTS and YS of the composites decrease as the volume fraction of NbC becomes lower. With a similar trend, the UTS and YS reach the minimum of 382.9 and 266.7 MPa, respectively, when the content of NbC is 5 vol.%. In terms of elongation, it also decreases gradually with the increase of NbC volume fraction, but the decrease is relatively small. The 5 vol.% NbC/H13 composite has the minimum elongation (2.6%).

Figure 10 shows SEM micrographs of longitudinal sections of the composites after tensile tests at room temperature. It can be seen from the figure that when there is deformation caused by external forces, the NbC phase is prone to stress concentration and micro-cracks. The NbC phase becomes a crack source, which offers paths for crack expansion, thus accelerating crack expansion and increasing the possibility of brittle fracture. When the content of NbC reaches 5 vol.% from 3 vol.%, the morphology of the NbC phase gradually changes to granular. When plastic deformation occurs, NbC absorbs the
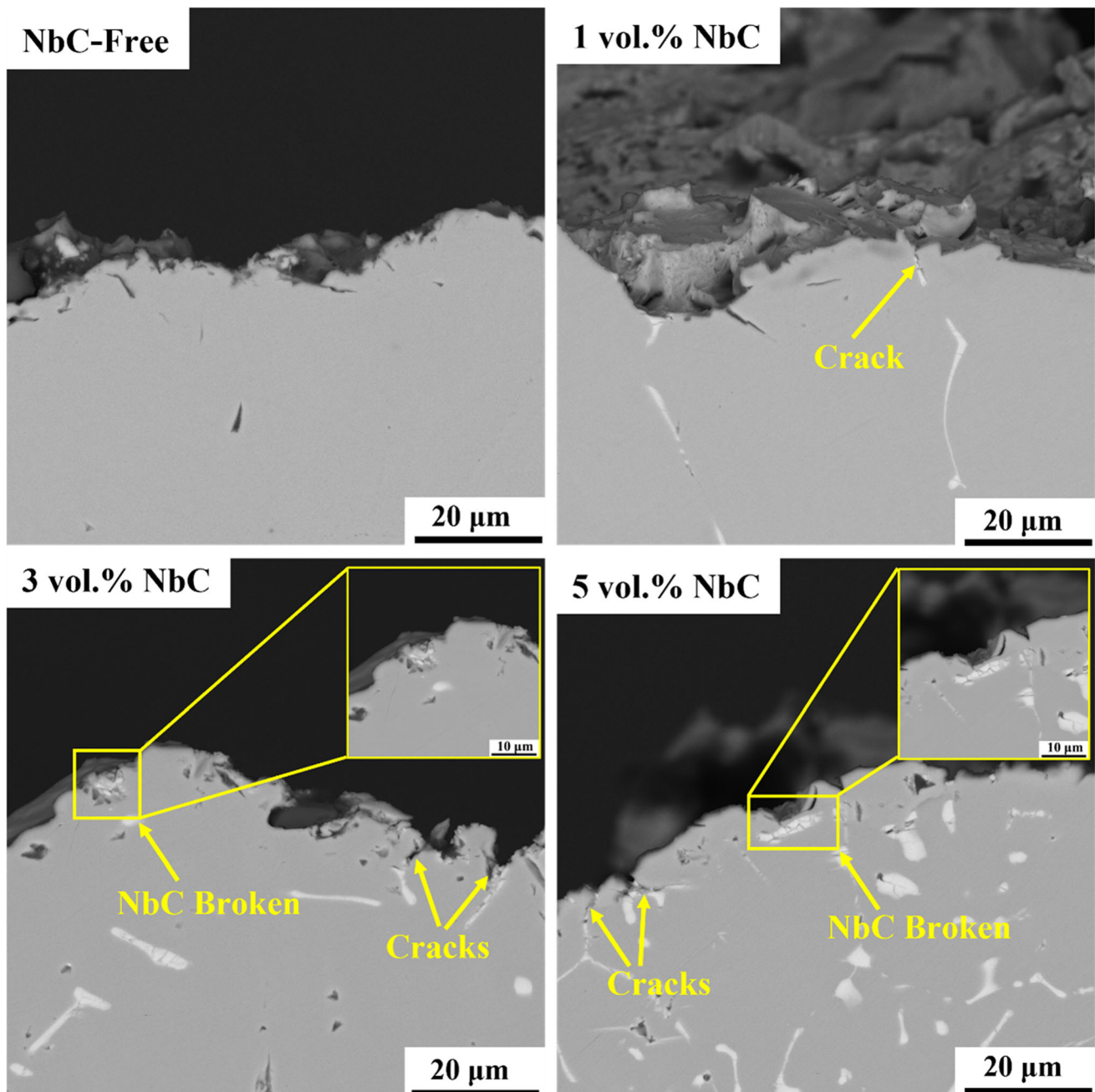
Fig. 10 SEM micrographs of longitudinal sections of NbC/H13 steel composites with different volume fractions experiencing tensile tests

energy generated during the deformation, resulting in broken granules, which reduces the process of crack extension.

3.4 Impact-Abrasive Wear Resistance

Figure 11 shows the volume loss and grinding process of the NbC-free composite and other ones. Obviously both the matrix and composites have suffered different volume losses. The volume loss of the matrix is the largest among all samples. Among the composites, the 1 vol.% NbC/H13 steel composite experiences the largest volume loss. It is because when the content of NbC is 1 vol.%, the NbC phase has a mesh-like structure, and it may fracture and peel off from the matrix with some of the metal matrix during the abrasive wear process. Moreover, the remaining broken NbC phase has higher
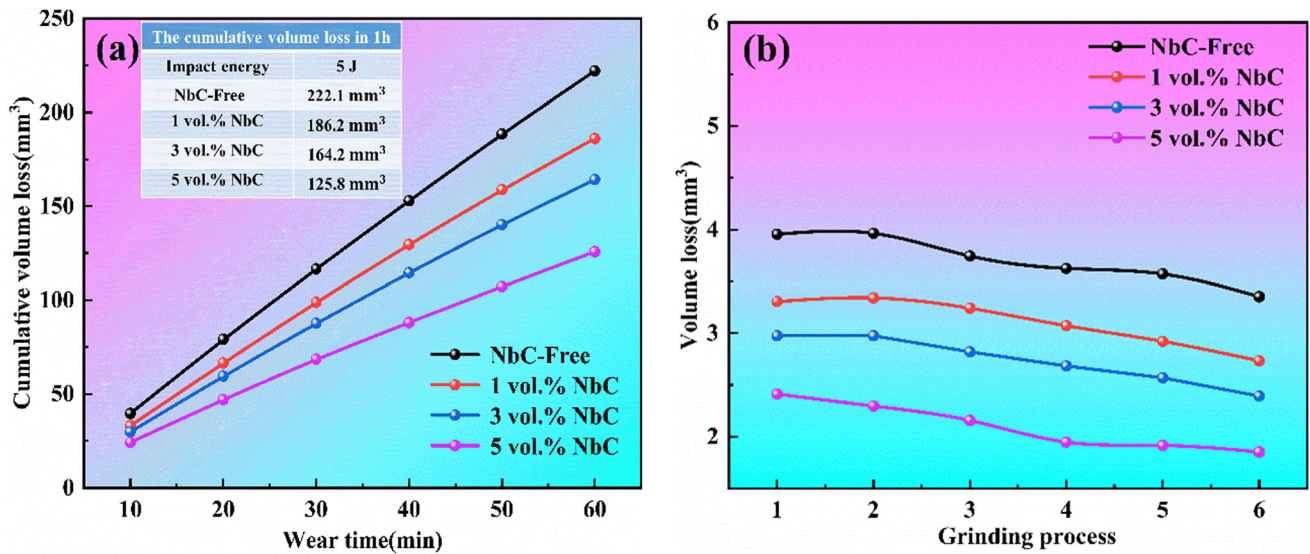
Fig. 11 (a) Volume loss of NbC/H13 steel composites with different volume fractions receiving abrasive wear and (b) grinding process

hardness than the matrix, so it functions as an abrasive, further aggravating the wear. In contrast, the 5 vol.% NbC/H13 steel composite is different. Although the generated phase has higher hardness, the NbC phase is gradually replaced by particles and more densely distributed with the increase of the content of NbC. Thus the sample is more wear-resistant and suffers minimal volume loss. After comparison, it was found that the composite with 5 vol.% Nb was 1.8 times more wear-resistant than the NbC-free one.
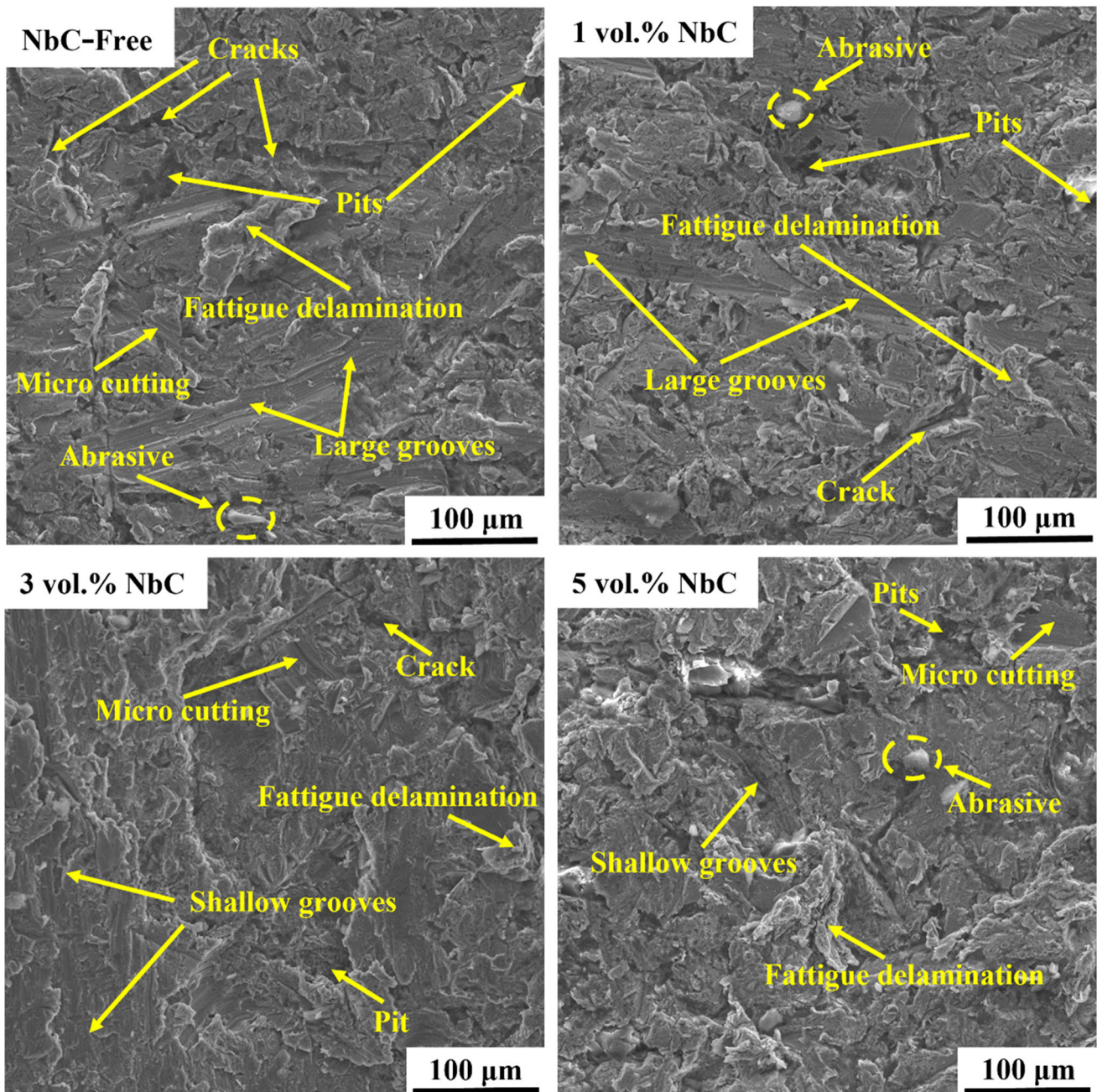
The wear morphology of the composites was analyzed by an SEM, as shown in Fig. 12. It shows that the matrix experiences relatively severe plastic deformation, and there are deep grooves on it after wear. This can be explained by the NbC phase. The phase resists the abrasive wear in the composites, and its high hardness protects the matrix from being cut by abrasive particles, thus greatly improving the wear resistance of the composite. In the NbC-free H13 steel, during impact wear, abrasives break into tiny fragments and the composite has difficulty in resisting the embedding of these tiny abrasive particles, resulting in more deep plow grooves, more serious fatigue spalling, and deeper gouges. As the NbC volume fraction reaches 5 vol.%, the distribution of the NbC phase becomes denser, which reduces the chance of direct contact between the matrix and abrasives, which makes it difficult for abrasives to go into the matrix. The number of craters and plough furrows in the composite gradually decreases, and plough furrows become shallow, which improves the wear resistance of the composite.

Figure 13 is SEM micrographs of longitudinal sections of the composites receiving impact wear. In the NbC-free sample, it cracked at a 5 J-impact, and tiny spalling pits appeared on the wear surface. Cracks can easily lead the wear surface to be

layered and peel, which is one of the most detrimental failure modes in the wear process (Ref 38). With the addition of NbC, the wear marks on the wear surface gradually become not that deep, which is attributed to the NbC. As the wear time increases, the NbC phase slowly protrudes to bear the wear and protect the matrix around it from being embedded by abrasives, while the matrix can provide good support for the phase. As the volume fraction of the NbC phase reaches 5 vol.%, its morphology changes. The NbC and the abrasives wear against each other, leading to the fragment of the NbC phase, thus reducing the spalling of the matrix and allowing the composite to gain optimum wear resistance.

The impact abrasive wear mechanism of the matrix and composites is shown in Fig. 14. The hardness of the steel matrix is often lower than the abrasives, the abrasives tend to damage the metal during the wear process. Thus deeper grooves are formed on the metal surface, and the steel matrix suffers from severe deformation, plowing, or micro-cutting due to the existence of abrasives and impact forces. At the same time, the abrasives are easily broken under the impact, and their fragments may go into the surface of the matrix, leading to more severe abrasive wear as the wear time increases. For NbC-reinforced composites, the hardness of the NbC phase is high, which can better resist abrasive wear on the metal matrix and enable composites to show better wear resistance. But when the volume fraction of NbC is too low, the phase tends to peel off from the metal matrix during wear and serves as a new abrasive during its fragment and spalling. This exacerbates the wear of the composite as the broken NbC phase has higher hardness than the metal matrix. When the volume fraction reaches 5 vol.%, the NbC phase changes from fine to coarse. During the wear process, the H13 steel matrix with lower hardness

Fig. 12 Secondary electron (SE) images of the abrasive wear morphology of NbC/H13 steel composites at different volume fractions

bears the wear first, which leads to the slow protrusion of NbC. Then the protruding part starts to bear wear and protect the matrix around it from being cut by abrasive particles, which is called the "shadow protection effect". Similarly, in the NbC-reinforced matrix, the matrix can provide good support for the NbC phase, and the two work together to protect the composites and give them optimal wear resistance (Ref 39).

4. Conclusions

In this paper, NbC/H13 steel composites were prepared through in-situ casting. The microstructure, mechanical properties, and wear properties of H13 steel matrix composites reinforced with NbC with different volume fractions were investigated, and the following conclusions were drawn.
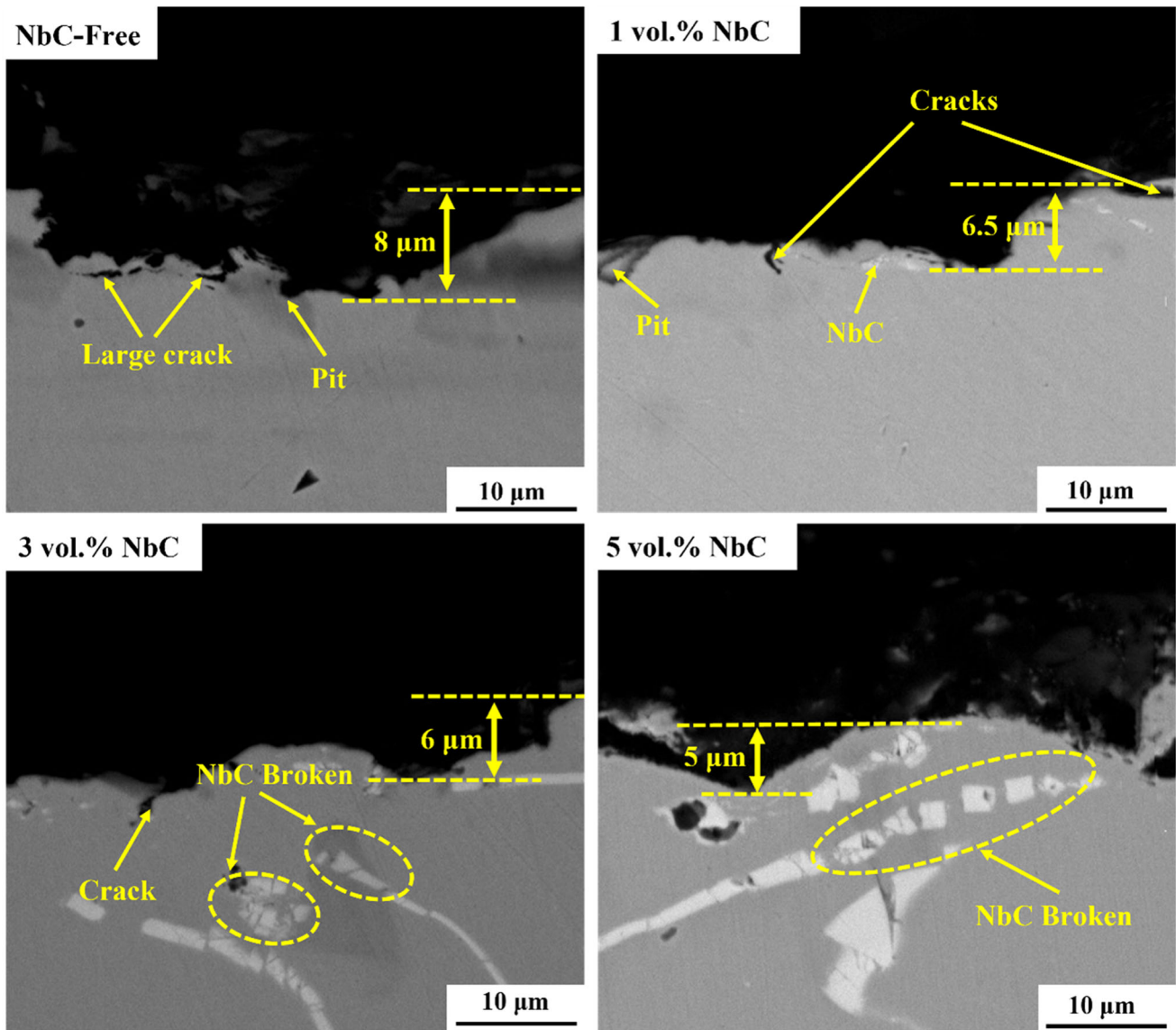
Fig. 13 SEM micrographs of longitudinal sections of different NbC/H13 steel composites receiving impact abrasive wear

(1) When the content of NbC was 1 vol.%, the NbC phase had a mesh-like structure, and it gradually changed from mesh-like to rod-like and then granular as the volume fraction increased to 3 and 5 vol.%, respectively.

(2) With the increase of the volume fraction of NbC, the hardness and modulus of the NbC phase grew higher, and the hardness and elastic modulus reached the maximum of 8.1 ± 0.9 and 246.8 ± 6.7 GPa, respectively, when the content of NbC reached 5 vol.%., and the mechanical properties decreased accordingly. In addition, the UTS, YS, and elongation reached the minimum of 382.9, 266.7 MPa, and 2.6%, respectively, when the content of NbC was 5 vol.%.

(3) When the hard NbC phase was added, it could well resist the abrasives from embedding in the metal matrix and reduce the wear loss caused by micro-cutting, which made the wear resistance of the composite at least 1.12 times higher than that of the NbC-free H13 steel.
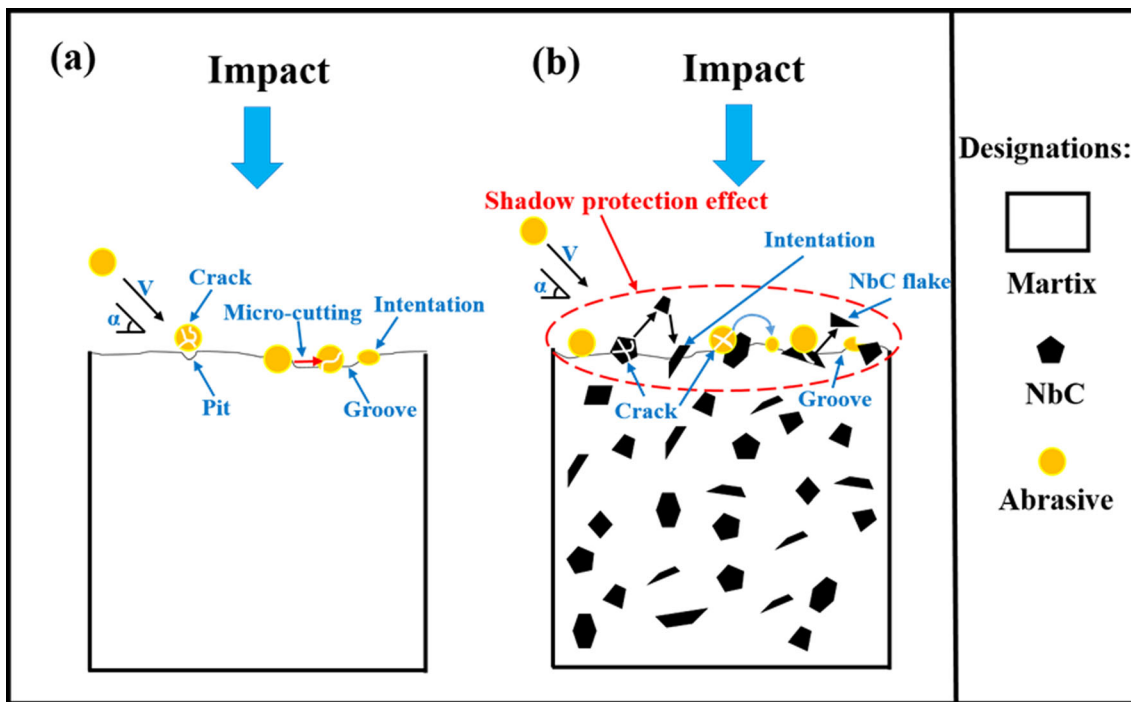
Fig. 14 Schematic illustration of the wear loss mechanism of the matrix and composites in SiO$_2$ sand: (a) matrix, (b) composites

Conflict of interest

The authors declare that they have no known competing financial interests or personal relationships that could have appeared to influence the work reported in this paper.

References

1. D. Merlini, D. Stocker, and M. Falanesca, The Ceneri Base Tunnel: Construction Experience with the Southern Portion of the Flat Railway Line Crossing the Swiss Alps, *Engineering*, 2018, **4**, p 235–248. https://doi.org/10.1016/j.eng.2017.09.004
2. F. Yang, H. Zhou, and C. Zhang, An Analysis Method for Evaluating the Safety of Pressure Water Conveyance Tunnel in Argillaceous Sandstone Under Water-Weakening Conditions, *Tunn. Undergr. Space Technol.*, 2020, **97**, p 103264. https://doi.org/10.1016/j.tust.2019.103264
3. G. Qi, W. Zhengying, and H. Fei, Comparison of the Mechanical Performance Between Two-Stage and Flat-Face Cutter Head for the Rock Tunnel Boring Machine (TBM), *J. Mech. Sci. Technol.*, 2015, **29**, p 2047–2058. https://doi.org/10.1007/s12206-015-0425-2
4. J.L. Cheng, Z.H. Jiang, and W.F. Han, Breakage Mechanism of Hard-Rock Penetration by TBM Disc Cutter After High Pressure Water Jet Precutting, *Eng. Fract. Mech.*, 2020, **240**, p 107320. https://doi.org/10.1016/j.engfracmech.2020.107320
5. W. Su, X. Li, and D. Jin, Analysis and Prediction of TBM Disc Cutter Wear When Tunneling in Hard Rock Strata: A Case Study of a Metro Tunnel Excavation in Shenzhen, China, *Wear*, 2020, **446**, p 203190. https://doi.org/10.1016/j.wear.2020.203190
6. X.H. Zhang, L.K. Lin, and Y.M. Xia, Experimental Study on Wear of TBM Disc Cutter Rings with Different Kinds of Hardness, *Tunn. Undergr. Space Technol.*, 2018, **82**, p 346–357. https://doi.org/10.1016/j.tust.2018.08.050
7. L. Wang, H. Li, and X. Zhao, Development of a Prediction Model for the Wear Evolution of Disc Cutters on Rock TBM Cutterhead, *Tunn. Undergr. Space Technol.*, 2017, **67**, p 147–157. https://doi.org/10.1016/j.tust.2017.05.003
8. E. Farrokh, Cutter Change Time and Cutter Consumption for Rock TBMs, *Tunn. Undergr. Space Technol.*, 2021, **114**, p 104000. https://doi.org/10.1016/j.tust.2021.104000
9. A.R. Chintha, Metallurgical Aspects of Steels Designed to Resist Abrasion, and Impact-Abrasion Wear, *Mater. Sci. Technol.*, 2019, **35**, p 1133–1148. https://doi.org/10.1080/02670836.2019.1615669
10. A.R. Chintha, K. Valtonen, and V.T. Kuokkala, Role of Fracture Toughness in Impact-Abrasion Wear, *Wear*, 2019, **428**, p 430–437. https://doi.org/10.1016/j.wear.2019.03.028
11. D. Tkalich, A. Kane, and A. Saai, Wear of Cemented Tungsten Carbide Percussive Drill-Bit Inserts: Laboratory and Field Study, *Wear*, 2017, **386–387**, p 106–117. https://doi.org/10.1016/j.wear.2017.05.010
12. S.L. Tang, Y.M. Gao, and Y.F. Li, Recent Developments in Fabrication of Ceramic Particle Reinforced iron Matrix Wear Resistant Surface Composite Using Infiltration Casting Technology, *Ironmak. Steelmak.*, 2014, **48**, p 633–639. https://doi.org/10.1179/1743281213y.0000000175
13. W. Theisen, A Novel PM-Wear Protection Method to Meet High Comminution Demands, *Wear*, 2001 https://doi.org/10.1016/s0043-1648(01)00630-5
14. P. Li, J. Gao, and M.Y. Gong, Effects of Manganese on Diffusion and Wear Behavior of ZTA Particles Reinforced Iron Matrix Composites in Vacuum, *Vacuum*, 2020, **177**, p 109408. https://doi.org/10.1016/j.vacuum.2020.109408
15. I. Dinaharan, Influence of Ceramic Particulate Type on Microstructure and Tensile Strengths of Aluminum Matrix Composites Produced Using Friction Stir Processing, *J. Asian Ceram. Soc.*, 2016, **4**, p 209–218. https://doi.org/10.1016/j.jascer.2016.04.002
16. C. Chen, Y. Xie, and X. Yan, Cold Sprayed WC Reinforced Maraging Steel 300 Composites: Microstructure Characterization and Mechanical Properties, *J. Alloy. Compd.*, 2019, **785**, p 499–511. https://doi.org/10.1016/j.jallcom.2019.01.135
17. K.E. Oksuz and Y. Sahin, Microstructure and Hardness Characteristics of Al$_2$O$_3$-B$_4$C Particle-Reinforced Cu Matrix Composites, *Acta Phys. Pol. A*, 2016, **129**, p 650–652.
18. J. Grabian and J. Wysocki, TIG-Bonding of AlSi9/SiC Composites, *Weld. Int.*, 2007, **21**, p 368–371. https://doi.org/10.1080/09507110701444891

19. C. Li, Y.F. Li, and J. Shi, The Effect of Multi-Arc Ion Plating NiCr Coating on Interface Characterization of ZrO_2-Al_2O_3 Ceramics Reinforced Iron-Based Composites, *Vacuum*, 2022, **196**, p 110758. https://doi.org/10.1016/j.vacuum.2021.110758

20. C.C. Degnan and P.H. Shipway, The Incorporation of Self-Propagating, High-Temperature Synthesis-Formed Fe-TiB_2 into Ferrous Melts, *Metall. Mater. Trans. A Phys. Metall. Mater. Sci.*, 2002, **33**, p 2973–2983. https://doi.org/10.1007/s11661-002-0282-3

21. D.H. Bacon, L. Edwards, and J.E. Moffatt, Fatigue and fracture of a 316 stainless steel metal matrix composite reinforced with 25% titanium Diboride, *Int. J. Fatigue*, 2013, **48**, p 39–47. https://doi.org/10.1016/j.ijfatigue.2012.09.016

22. L.S. Zhong, Y.H. Xu, and F.X. Ye, In Situ NbC Particulate-Reinforced Iron Matrix Composite: Microstructure and Abrasive Wear Characteristics, *Tribol. Lett.*, 2012, **47**, p 253–259. https://doi.org/10.1007/s11249-012-9977-9

23. H. Wu, S.R. Huang, and C.M. Zhao, Microstructures and Mechanical Properties of In-Situ FeCrNiCu High Entropy Alloy Matrix Composites Reinforced with NbC Particles, *Intermetallics*, 2020, **127**, p 106983. https://doi.org/10.1016/j.intermet.2020.106983

24. Y.-B. Cao, H.-T. Ren, and C.-S. Hu, In-Situ Formation Behavior of NbC-Reinforced Fe-Based Laser Cladding Coatings, *Mater. Lett.*, 2015, **147**, p 61–63. https://doi.org/10.1016/j.matlet.2015.02.026

25. W.H. Kan, Z.J. Ye, and Y. Zhu, Fabrication and Characterization of Microstructure of Stainless Steel Matrix Composites Containing up to 25 vol% NbC, *Mater. Charact.*, 2016, **119**, p 65–74. https://doi.org/10.1016/j.matchar.2016.07.019

26. R. Yousefian, E. Emadoddin, and S. Baharnezhad, Manufacturing of the Aluminum Metal-Matrix Composite Reinforced with Micro- and Nanoparticles of Tio_2 Through Accumulative Roll Bonding Process (ARB), *Rev. Adv. Mater. Sci.*, 2018, **55**, p 1–11.

27. F. Shehata, A. Fathy, and M. Abdelhameed, Preparation and Properties of Al_2O_3 Nanoparticle Reinforced Copper Matrix Composites by In Situ Processing, *Mater. Des.*, 2009, **30**, p 2756–2762. https://doi.org/10.1016/j.matdes.2008.10.005

28. L.S. Zhong, Y.H. Xu, and X.J. Liu, Study on NbC Particulate-Reinforced Iron Matrix Composite Produced In Situ, *J. Mater. Sci.*, 2011, **46**, p 2814–2819. https://doi.org/10.1007/s10853-010-5157-1

29. W.H. Kan, G. Proust, and V. Bhatia, Slurry Erosion, Sliding Wear and Corrosion Behavior of Martensitic Stainless Steel Composites Reinforced In-Situ with NbC Particles, *Wear*, 2019, **420**, p 149–162. https://doi.org/10.1016/j.wear.2018.09.013

30. E.D. Wen, R.B. Song, and C.H. Cai, Study of the Three-Body Impact Abrasive Wear Behaviour of a Low Alloy Steel Reinforced with Niobium, *J. Manuf. Process.*, 2019, **46**, p 185–193. https://doi.org/10.1016/j.jmapro.2019.08.026

31. M.J. Chao, W.L. Wang, E.J. Liang et al., Microstructure and Wear Resistance of TaC Reinforced Ni-Based Coating by Laser Cladding, *Surf. Coat. Technol.*, 2008, **10**, p 1918–1922. https://doi.org/10.1016/j.surfcoat.2007.08.021

32. J. Wang, C. Li, M. Zeng et al., Microstructural Evolution and Wear Behaviors of NbC-Reinforced Ti-Based Composite Coating, *Int. J. Adv. Manuf. Technol.*, 2020, **107**, p 2397–2407. https://doi.org/10.1007/s00170-020-05198-w

33. N.N. Wang, Y.H. Xu, X.J. Liu et al., Analysis on Reaction Process and Thermo-dynamics of In-situ NbC/Fe Composites, *Mater. Heat Treat.*, 2010, **24**, p 4. https://doi.org/10.3969/j.issn.1001-3814.2010.24.027

34. D. Wu, J. Zhang, and J.C. Huang, Grain-Boundary Strengthening in Nanocrystalline Chromium and the Hall-Petch Coefficient Of Body-Centered Cubic Metals, *Scripta Mater.*, 2013, **68**, p 118–121. https://doi.org/10.1016/j.scriptamat.2012.09.025

35. H. Moon, B.K. Kim, and S.J.L. Kang, Growth Mechanism of Round-Edged NbC Grains in Co Liquid, *Acta Mater.*, 2001, **49**, p 1293–1299. https://doi.org/10.1016/s1359-6454(00)00394-3

36. S.G. Du, S.L. Wang, and W.T. Xu, Characterizing Micromechanical Properties of Friction Welding Interface Between TiAl Alloy and GH3039 Superalloy, *Materials*, 2020, **13**, p 1–11. https://doi.org/10.3390/ma13092072

37. E. Pagounis and V.K. Lindroos, Processing and Properties of Particulate Reinforced Steel Matrix Composites, *Mater. Sci. Eng. A Struct. Mater. Prop. Microstruct. Process.*, 1998, **246**, p 221–234. https://doi.org/10.1016/s0921-5093(97)00710-7

38. B.G. Liu, W. Li, and X.W. Lu, An Integrated Model of Impact-Abrasive Wear in Bainitic Steels Containing Retained Austenite, *Wear*, 2019, **440**, p 203088. https://doi.org/10.1016/j.wear.2019.203088

39. Z. Li, Y. Jiang, and R. Zhou, Dry Three-Body Abrasive Wear Behavior of WC Reinforced Iron Matrix Surface Composites Produced by V-EPC Infiltration Casting Process, *Wear*, 2007, **262**, p 649–654. https://doi.org/10.1016/j.wear.2006.07.009